PCCP

ROYAL SOCIETY OF CHEMISTRY

PAPER

View Article Online
View Journal | View Issue

Cite this: *Phys. Chem. Chem. Phys.*, 2021, **23**, 26806

Synthesis of 2D semiconducting single crystalline Bi_2S_3 for high performance electronics

Youngchan Kim,[a] Euihoon Jeong,[b] Minwoong Joe[c] and Changgu Lee *[bc]

Received 19th August 2021,
Accepted 4th November 2021

DOI: 10.1039/d1cp03815j

rsc.li/pccp

2-Dimensional (2D) semiconducting materials are attractive candidates for future electronic device applications due to the tunable bandgap, transparency, flexibility, and downscaling to the atomic level in material size and thickness. However, 2D materials have critical issues regarding van der Waals contact, interface instability and power consumption. In particular, the development of semiconducting electronics based on 2D materials is significantly hindered by a low charge-carrier mobility. In order to improve the critical shortcoming, diverse efforts have been made in synthesis and device engineering. Here, we propose a synthesis method of single crystalline 2D Bi_2S_3 by chemical vapor deposition for high performance electronic device applications. The ion-gel gated field effect transistor with the as-grown Bi_2S_3 on the SiO_2 substrate exhibits a high mobility of 100.4 $cm^2\ V^{-1}\ S^{-1}$ and an on–off current ratio of 104 under a low gate voltage below 4 V at room temperature without chemical doping and surface engineering. The superior performance is attributed to the high crystal quality of Bi_2S_3 that shows low sulfur vacancies and atomic ratio close to the ideal value (2 : 3) under a rich sulfur growth process using H_2S gas instead of sulfur powder. The synthesis method will provide a platform to realize high performance electronics and optoelectronics based on 2D semiconductors.

1. Introduction

Field effect transistors (FETs) based on silicon are one of the main components of modern electronic integrated circuit and high-speed electronic devices due to their high charge-carrier mobility and low power consumption. Silicon-based FETs have been steadily improved and dramatically developed in fabrication processes for decrease of cost and improvement of electronic performance to date. Recently, the channel size of FETs has reached its theoretical limitation of scaling of less than 10 nm. The short channel of FETs results in critical issues such as high-power consumption, heat dispassion, high contact resistance and leakage current. Alternative materials are required to overcome the limitations and problems in conventional silicon-based transistors.

Two-dimensional (2D) materials such as graphene, BN, and MoS_2 have been attracting great attention due to their unique physical and chemical properties.[1–5] Among these materials, 2D semiconducting materials such as MoS_2, WSe_2 and phosphorene have high potential in future electronic device development because of their atomic-scale thickness, high flexibility, and controllable band gap.[5–10]

However, common 2D semiconducting materials have critical issues such as high contact resistance, interface instability and high power consumption.[11–15] In particular, they exhibit low intrinsic charge–carrier mobilities (0.1–10 $cm^2\ V^{-1}\ S^{-1}$) at room temperature that critically impedes their application in electronic devices.[16–18,29] Although phosphorene exhibits outstanding electrical mobility (1000 $cm^2\ V^{-1}\ S^{-1}$), it is not an appropriate candidate for next-generation electronic devices due to significant instability in the air.[19,20]

Bi_2S_3 (bismuth sulfide) is an anisotropic orthorhombic structured 2D semiconducting material.[21,22] It exhibits superior optoelectronic properties due to unique physical properties such as strong spin–orbit coupling and a band gap of 1.3 eV.[23–25] It also possesses excellent thermoelectric properties because of small effective carrier masses, a high Seebeck coefficient and low thermal conductivity.[21,26] Above all, Bi_2S_3 presents theoretically a high electron mobility of 200 $cm^2\ V^{-1}\ S^{-1}$ and a hole mobility of 1100 $cm^2\ V^{-1}\ S^{-1}$ that can be applied in high performance electronic devices.[27] However, electronic devices based on synthesized Bi_2S_3 have shown a relatively low mobility like other 2D semiconducting materials owing to low crystal quality and unintentional impurities and vacancy defects.[28,29]

We have developed a synthesis method for single crystalline Bi_2S_3 by chemical vapor deposition (CVD). Bi_2S_3 was grown

[a] *School of Mechanical and Automotive Engineering, Kyungsung University, 309, Suyeong-ro, Nam-gu, Busan, Republic of Korea. E-mail: ykim2020@ks.ac.kr*
[b] *SKKU Advanced Institute of Nanotechnology (SAINT), Sungkyunkwan University, Seobu-ro, Jangan-gu, Suwon, Gyeonggi-do, 2066, Republic of Korea. E-mail: dmlgns664@gmail.com, peterlee@skku.edu*
[c] *School of Mechanical Engineering, Sungkyunkwan University, Seobu-ro, Jangan-gu, Suwon, Gyeonggi-do, 2066, Republic of Korea*

Table 1 Comparisons of mobility and current on/off ratio between the synthesized Bi_2S_3 with other conventional 2D materials using the chemical vapor deposition (CVD) method

2D materials (CVD)	Progress	Layer	Mobilities ($cm^2\ V^{-1}\ S^{-1}$)	On/off ratio	Ref.
MoS_2	MoO_3 + S (powder)	Monolayer	~4	$\sim 10^7$	Van Der Zande *et al.*, Nature materials, (2013)[41]
WS_2	H_2WO_4 + NaCl + S (powder)	Monolayer	~28	—	F. Reale *et al.*, Scientific reports, (2017)[42]
ReS_2	Re + S (powder)NH_4ReO_4 + S (powder)	Monolayer bilayer	~9	$\sim 10^6$	X. He *et al.*, Small, (2015)[43]
			$\sim 7.2 \times 10^{-2}$	$\sim 10^3$	K. Keyshar *et al.*, Advanced Materials, (2015)[44]
Bi_2S_3 (nano wire)	Bi_2O_3 + S (powder)	—	~0.563	$\sim 10^3$	F. Lu *et al.*, ChemPhysChem, (2015)[45]
Bi_2S_3 (nano sheet)	Bi + S (powder)	—	~28	$\sim 10^3$	K. A. Messalea *et al.*, Advanced Materials Interfaces, (2020)[46]
Bi_2S_3 (single crystal)	Bi_2O_3 + H_2S (gas)	Few layer	~100.4	$\sim 10^4$	This work

directly on a SiO_2 substrate using Bi_2O_3 powder and H_2S gas instead of conventional sulfur powder. Sulfur powder is broadly used to synthesize 2D materials such as MoS_2, WS_2 and ReS_2 (Table 1). However, it is difficult to provide a steady density of sulfur during the growth process due to a solid state material. Moreover, the CVD method using sulfur powder can result in high sulfur vacancies which is the main reason for the low crystallinity of 2D materials such as MoS_2, WS_2 and ReS_2.

Previous reports have demonstrated that an annealing process under sulfur supply can improve the quality of crystals by lowering the ratio of sulfur vacancies in the crystal structures.[30,31] H_2S is the ideal precursor for the CVD method because of the gas phase material that can exactly control the density and supply duration of the precursor. H_2S was used to improve the crystallinity and solve the critical problem of sulfur vacancies of 2D materials such as MoS_2 and WS_2, because it can provide a steady and rich supply of sulfur during the process of growth. X-ray photoelectron spectroscopy (XPS) proved an atomic ratio of ideal value (2 : 3) that suggests high crystal quality with few sulfur defects. The single crystallinity and high crystal quality of Bi_2S_3 were confirmed by high-resolution transmission microscopy (HR-TEM). The smooth surface properties without impurities were revealed by atomic force microscopy (AFM). Above all, an ion-gel gated transistor based on as-grown Bi_2S_3 exhibited a high charge-carrier mobility of 100.4 $cm^2\ V^{-1}\ S^{-1}$ and an on–off ratio of 104 under a low gate voltage below 4 V at room temperature without chemical treatments and surface engineering that demonstrate high crystal quality of Bi_2S_3. These results demonstrate the feasibility of application of synthesized Bi_2S_3 in high performance and low voltage electronics and optoelectronics.

2. Results and discussion

2.1. Synthesis and improvement of the crystallinity of Bi_2S_3 using the LPCVD system

Fig. 1(a) shows a schematic diagram of the experimental set-up for synthesis.

As depicted in the figure, 2D Bi_2S_3 multilayer flakes were synthesized in a vacuum quartz tube in a furnace chamber under low pressure (~10–3 torr). CVD method was carried out

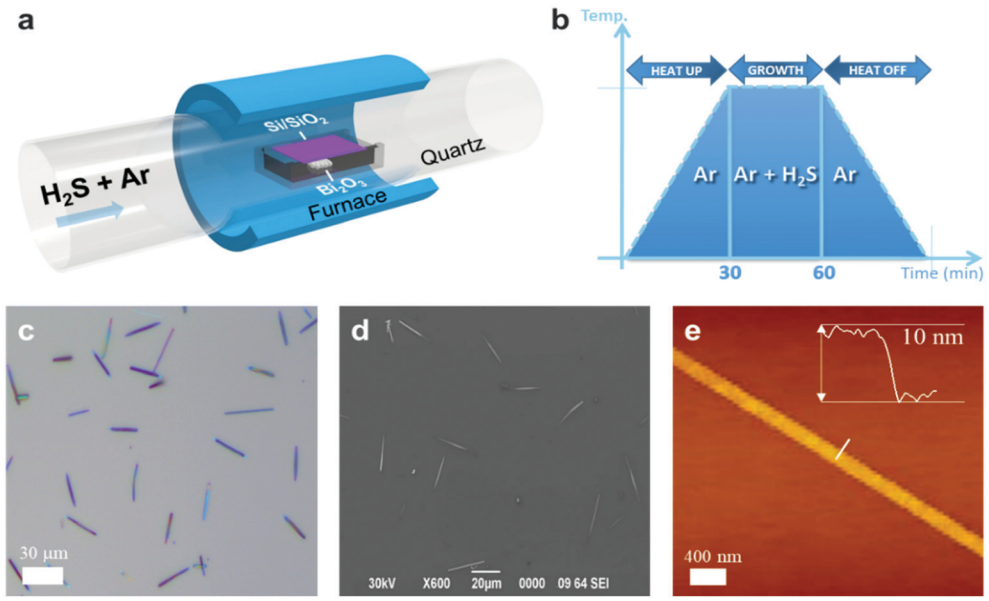

Fig. 1 The synthesis method of Bi_2S_3 and its characterization. (a) Schematic illustration of experimental set-up of Bi_2S_3, (b) diagram of synthesis process of Bi_2S_3, (c) OM image of as-grown Bi_2S_3, (d) SEM image of as-grown Bi_2S_3, and (e) AFM image and height profile of as-grown Bi_2S_3.

using H_2S and Bi_2O_3 powder as precursors and Ar gas was used as a transporting material in whole CVD process. Bi_2S_3 was directly grown on a SiO_2/Si substrate (300 nm SiO_2) by sulfurization of Bi_2O_3 after injection of H_2S gas (Fig. 1(a and b)). During the whole growth process, the density and supply duration of H_2S gas were exactly adjusted using a mass flow controller and CVD system. While sulfur powder is rapidly vaporised within several min, H_2S can provide a rich and steady sulfur environment until the end of the duration of growth. Although Bi_2S_3 can be synthesized within 10 min, the duration of H_2S gas supply increased up to 30 min including annealing process to reduce the sulfur vacancies and improve crystal quality.

2.2. Characterization and structure of Bi_2S_3

Fig. 1(c) and (d) show optical and electron microscopy images of Bi_2S_3 multilayer crystals which were grown on the SiO_2/Si substrate. The optical microscope image exhibits the contrast of multilayer Bi_2S_3 with the size of 10–50 micrometers. Also, the shape of synthesized Bi_2S_3 presents a highly anisotropically structured 1D nanowire. AFM measurements were performed to observe surface states and thicknesses as shown in Fig. 1(e).

Fig. 1(e) reveals the highly uniform and clean surface of Bi_2S_3 crystals without chemical residue and critical defects. The synthesized Bi_2S_3 samples show a thickness of about 10 nm and a width of about 200 nm.

Raman spectroscopy was used to characterize qualitative physical properties of Bi_2S_3 samples. As shown in Fig. 2(a), the Raman spectrum was obtained from the sample with approximately 10 nm thickness under a 532 nm wavelength laser and excitation power of 1 mW. The Raman system was calibrated using the Si peak at 520 cm^{-1}. The Raman spectrum shows well-defined main peaks at 185 and 235 cm^{-1} of A_g phonon mode and 260 cm^{-1} of B_{1g} phonon mode.[32] The A_g and B_{1g} vibration modes are associated with transverse and longitudinal optical phonons respectively. These peak positions match well with those values reported in both of previous theoretical works and experimental results.[33] PL spectroscopy was also performed using a 532 nm excitation source. To avoid thermal damage from laser irradiation, 1 mW of power was used for this work. The relatively weak signal of the PL spectrum results from a smaller width of the Bi_2S_3 sample ($\sim$200 nm) than the spot size of the Raman laser ($\sim$1 μm). As shown in Fig. 2(b), the PL spectrum has the main peak at 917 nm (1.33 eV) which corresponds well to the expected value of the optical band gap.[34,35]

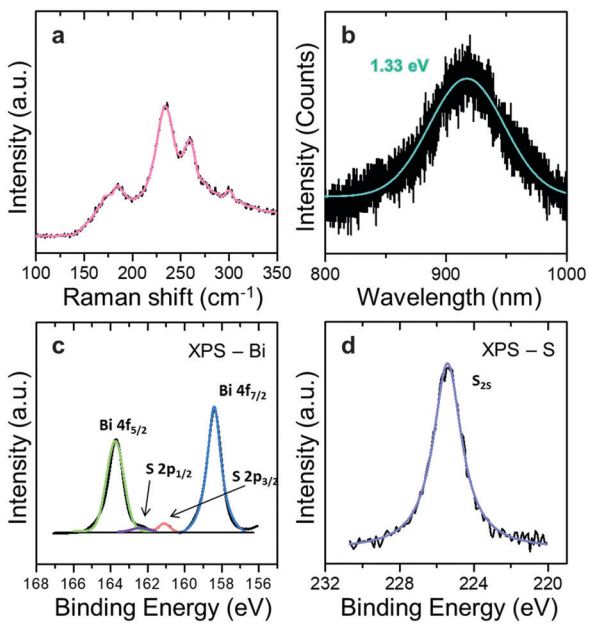

Fig. 2 Characterization of optical properties and stoichiometry analysis of Bi_2S_3 (a) Raman spectrum of Bi_2S_3, (b) PL spectrum of Bi_2S_3, (c) XPS spectrum of Bi 4f peaks and S 2p peaks, and (d) XPS spectrum of S 2s peaks.

XPS measurements were carried out to characterize the chemical stoichiometry of the synthesized Bi_2S_3 crystals and prove low sulfur vacancies of Bi_2S_3 crystals (Fig. 2(c) and (d)). To obtain exact peak values, the experimental data were fitted with 4 peaks as shown in Fig. 2(c). The 4f spectrum of Bi^{3+} presents dominant peaks at 163.7 and 158.4 related to $4f_{5/2}$ and $4f_{7/2}$ respectively.

Similarly, Fig. 2(c) reveals two peaks at 162.3 and 161.1 eV representing S $2p_{1/2}$ and S $2p_{2/3}$. In Fig. 2(d), the 2s spectrum of S exhibits the peak at 225.3 eV. These results correspond well to the chemical bond between sulfur and bismuth of Bi_2S_3.[33] The Bi 4f orbitals, which result from inherent oxide in Bi_2O_3 can appear at high binding energy levels.[36]

The Bi 4f spectrum shows no signal arising from the Bi_xO_y radicals or Bi_2O_3 residues. The atomic ratio of Bi to S is about 0.67 (Fig. 2(c) and (d)), which closely corresponds to the ideal stoichiometry of Bi_2S_3 and proves the presence of a few sulfur vacancies that result in critical low crystal quality. Furthermore, this result shows lower ratio of sulfur vacancies than CVD-grown Bi_2S_3 using sulfur powder.[37]

The electronic band structure of bulk Bi_2S_3 is plotted in Fig. 3. It displays a semiconducting character with a bandgap of 1.29 eV, in excellent agreement with the previously reported value of 1.3 eV as well as our PL peak value of 1.33 eV.[47] The carrier effective mass is calculated by a parabolic fit to the band edge. The hole and electron effective mass from VBM and CBM are 0.39 m_0 and 0.25 m_0, respectively, where m_0 is the free electron mass. Compared with the value of MoS_2 ($\approx$ 0.5 m_0), such a smaller electron effective mass suggests a comparable or higher electron mobility than that of MoS_2 (10–50 $cm^2\ V^{-1}\ S^{-1}$).[48]

HR-TEM was used to analyze the crystal structure and evaluate the crystalline quality of a synthesized Bi_2S_3 sample. The Bi_2S_3 flakes synthesized on the SiO_2/Si substrate were coated with polymethylmethacrylate (PMMA) in a spin-coater. The PMMA coating with the flakes was removed from the substrate in a buffered oxide etchant (BOE) and rinsed in deionized water (DIW) several times.

The PMMA-supported Bi_2S_3 was transferred onto a TEM copper grid. PMMA was removed in acetone solution and the grid was rinsed in IPA several times. Fig. 4(a) shows the image of HR-TEM of a Bi_2S_3 flake transferred onto the copper TEM

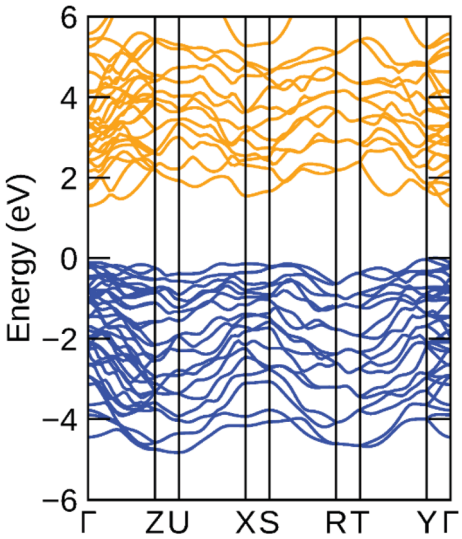

Fig. 3 Electronic band structure of bulk Bi_2S_3. Blue/orange lines for valence/conduction band. The VBM is set to be E = 0.

grid. Fig. 4(b) and (c) show the selected area electron diffraction (SAED) pattern and the HR-TEM image of the Bi_2S_3 flake, respectively. The SAED pattern in Fig. 4(b) presents a periodic orthogonal feature that is associated with a classical anisotropic orthorhombic structure of Bi_2S_3.

HR-TEM image shows no impurities and defects in the Bi_2S_3 crystal. Above all, the SAED pattern reveals a high-quality and perfect single crystal of a synthesized Bi_2S_3 flake. The diffraction points indicate the lattice planes in the SAED pattern and the (001) plane is perpendicular to the (020) plane.[38] This result is in good agreement with the lattice structure of Bi_2S_3 which is the orthorhombic crystal system with the lattice parameters of a = 0.112 nm, b = 1.125 nm, c = 0.397 nm, $\alpha = 90^\circ$, $\beta = 90^\circ$, $\gamma = 90^\circ$ as shown in Fig. 4(d).[39,40] Also, the low magnification image of HR-TEM in Fig. 4(C) demonstrates the anisotropic growth of Bi_2S_3 along a main axis of the [001] direction which is perpendicular to the [010] direction due to the anisotropic orthorhombic structure of Bi_2S_3 (Fig. 4(d)).

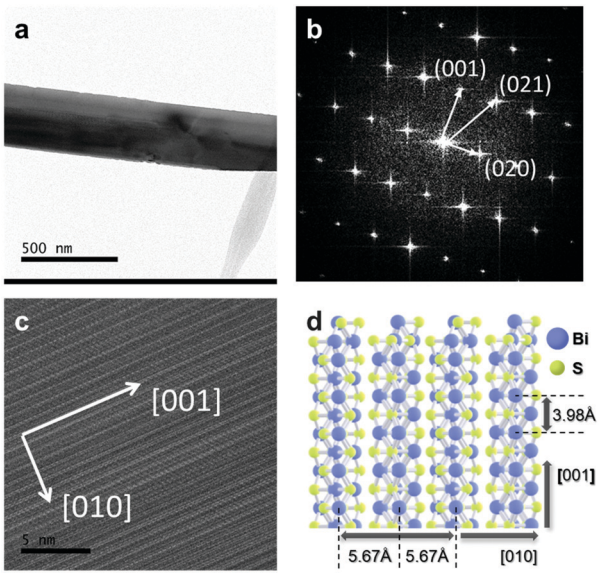

Fig. 4 Structure analysis of Bi_2S_3. (a) TEM image of Bi_2S_3 on a TEM grid, (b) SAED patterns of single crystalline Bi_2S_3, (c) HRTEM image of anisotropic Bi_2S_3 structure, and (d) schematic illustration of Bi_2S_3 crystal structure.

2.3. Electrical performance of a Bi_2S_3 FET

A FET was fabricated to evaluate the electronic properties of the synthesized Bi_2S_3 sample.

In this work, an as-grown multilayer Bi_2S_3 flake was used for fabrication as shown in Fig. 5(a) and (b). As shown in Fig. 5(a), 5 nm Cr and 50 nm Au as the electrode were deposited using an e-beam evaporator. The gate insulator was made by drop-casting an ionic liquid onto the Bi_2S_3 flake (Fig. 5(b) and (c)). The ion-gel solution consists of a poly(ethylene glycol) diacrylate (PEG-DA) monomer, a 2-hydroxy-2-methylpropiophenone (HOMPP) initiator, and a 1-ethyl-3-methylimidazolium bis(trifluoromethylsulfonyl)imide (EMIM : TFSI) ionic liquid with a weight ratio of 2 : 1 : 22. In Fig. 5(d), the transfer characteristics of the ion-gel gated FETs exhibited n-type behavior, which is consistent with previous reports. The field effect mobility can be calculated using the equation $\mu = (L/WV_DC_{ion\text{-}gel})\ (\Delta I_D/\Delta V_G)$, where L, W, and $C_{ion\text{-}gel}$ are the channel length, the channel width, and capacitance of the ion-gel gate dielectric.

The value of $\Delta I_D/\Delta V_G$ was obtained from the slope of the transfer characteristic curve plotted in Fig. 5(d). The FET exhibited a high electron mobility of 100.4 $cm^2\ V^{-1}\ S^{-1}$, and a high current on/off ratio of $\sim 10^4$ at V_D = 1 V, which are superior to those of other conventional 2D materials such as

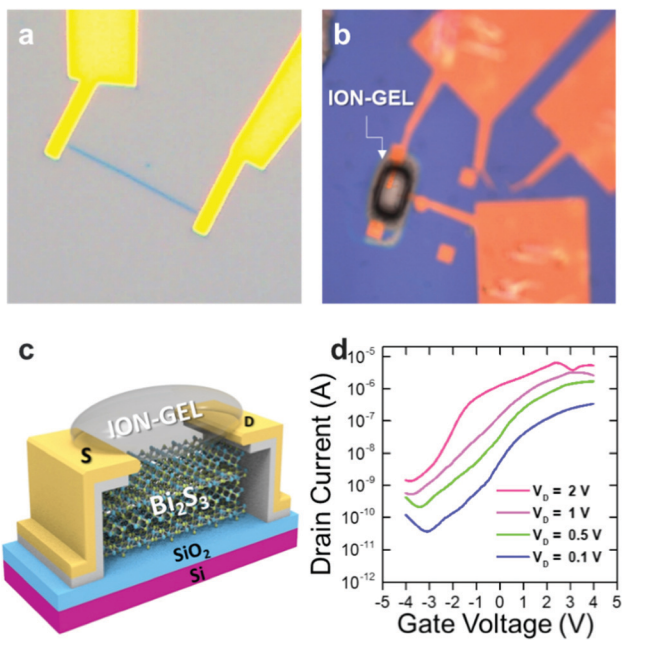

Fig. 5 Electronic properties of Bi_2S_3: (a) OM image of FET based on as-grown Bi_2S_3, (b) OM image of the ion-gel gated transistor of Bi_2S_3, (c) schematic diagram of ion-gel gated Bi_2S_3 FET, (d) transfer characteristics of Bi_2S_3 transistor.

MoS_2, WS_2 and ReS_2 as well as those of the previously reported Bi_2S_3 (Table 1). The excellent electronic device performance again proves the high crystallinity of the synthesized flakes and demonstrates the feasibility of practical and high-performance electronic device applications.

3. Experimental

3.1. Synthesis of Bi_2S_3

Bi_2O_3 powder (99.9%, Sigma Aldrich) was used as the precursor for the synthesis of Bi_2S_3. Bi_2S_3 was grown in a vacuum quartz tube in a furnace under low pressure ($\sim$103 torr). Before synthesis, SiO_2/Si (300 nm SiO_2) wafer was cleaned in acetone and isopropyl alcohol (IPA) and then rinsed in DIW several times. A mass of Bi_2O_3 5 mg powder in a quartz boat was put onto the edge of the furnace and covered by SiO_2/Si wafer. The furnace was heated up to 550 °C for 30 min and then H_2S gas was injected for sulfurization of Bi_2O_3 for 30 min. The furnace chamber was cooled down to room temperature. Ar gas was injected over the whole process.

3.2. Characterization of synthesized Bi_2S_3

Raman and PL spectroscopy was carried out at 532 nm laser wavelength, and 1 mW laser power, which avoids thermal damage to samples. The Raman instrument (NTMDT AFM-Raman spectroscope) was calibrated using a Si peak of 520 cm^{-1} before measurement. XPS was performed to determine the chemical stoichiometry and bonding states of Bi_2S_3 with an Al Kα X-ray source (ESCALAB 220i-XL, VG Scientific Instruments). AFM was used for surface analysis and measurement of the thickness of the samples. AFM measurements (Seiko instrument) were taken with a Si tip (NT-MDT). To make the TEM sample, a Bi_2S_3 on SiO_2/Si wafer was coated with polymethylmethacrylate (PMMA) in a spin-coater. It was immersed in BOE solution to remove SiO_2 and then was rinsed in DIW several times. The PMMA-supported Bi_2S_3 was transferred onto a TEM copper grid and the PMMA was removed in acetone for 30 min and rinsed in IPA several times. The TEM images and SAED patterns were obtained using a JEM-2100F, Cs corrector.

3.3. Structure relaxation and electronic band structure calculations

All the DFT calculations were performed using the Vienna *ab initio* Simulation Package (VASP).[49] For the ion–electron interaction, projector augmented wave (PAW) pseudopotentials were used. For the exchange–correlation functional, the Perdew–Burke–Ernzerhof (PBE) type generalized gradient approximation (GGA) was adopted.[50] The van der Waals interactions were described by the DFT-D3 Grimme method.[51] The Γ-centered k-mesh of 4 × 12 × 5 (9 × 25 × 9) and the plane-wave energy cutoff of 600 eV were set for the structural optimization (electronic band structure calculation). The calculated lattice constants of the relaxed bulk Bi_2S_3 are a = 11.12 Å, b = 11.29 Å and c = 4.00 Å, in very good agreement with the experimental values (a = 11.2 Å, b = 11.25 Å and c = 3.97 Å).

3.4. Device fabrication

A FET based on as-grown Bi_2S_3 was fabricated using e-beam-lithography. The metal electrodes of Cr/Au (5/50 nm) were deposited by using an e-beam evaporator. To make the gate insulator, the ionic liquid was drop-cast onto the FET. The gate dielectric layer was formed by drop-casting an ion-gel solution comprising poly(ethyleneglycol) diacrylate (PEGDA, Sigma-Aldrich), 2-hydroxy-2-methylpropiophenone (HOMPP, Sigma Aldrich), and 1-ethyl-3-methylimidazolium bis (trifluoromethanesulfonyl) imide ([EMIM][TFSI]) ionic liquid (Merck) in a weight ratio of 2 : 1 : 22. After drying, the ion gel layer in a patterned photomask was exposed to UV light (365 nm, 100 mW cm^{-2}) for five seconds. The area exposed to UV light became chemically crosslinked, while the unexposed region was removed by rinsing in DIW.

4. Conclusions

In conclusion, we have developed the CVD method for the synthesis of single crystalline $Bi2S_3$. The crystals have the shapes of 1-dimensional nanowires or nanorods with a width of $\sim$200 nm and a thickness of tens of nanometers. TEM and SAED patterns revealed anisotropic properties and high crystallinity in the orthorhombic structure of Bi_2S_3. The optical band gap of Bi_2S_3 ($\sim$1.33 eV) was confirmed by PL spectroscopy. AFM and SEM images showed clean and uniform surfaces of Bi_2S_3. Above all, ion-gel gated FETs based on as-grown Bi_2S_3 displayed superior electronic properties with a charge carrier mobility of 100.4 $cm^2\ V^{-1}\ S^{-1}$, a current on/off ratio of $\sim 10^4$ and a low voltage operation below 4 V. The CVD method to grow Bi_2S_3 single crystals paves a new way for high performance electronics with 2D semiconducting materials.

Author contributions

Y. K. developed the synthesis method of Bi_2S_3 and carried out the analysis of CVD-grown Bi_2S_3, M. J. conducted the electronic band structure calculation of Bi_2S_3 and E. J. fabricated the device of Bi_2S_3 and conducted the electrical test. All authors contributed the discussion and preparation of the manuscript.

Conflicts of interest

There are no conflicts to declare.

Acknowledgements

This study was supported by the Basic Science Research Program (2021R1F1A1051987, 2016K1A1A2912707, 2018R1A6A3A11047867, 2020R1A2C2014687, and 2019R1I1A1A01061466) through the National Research Foundation of Korea (NRF) and the KISTI grant (KSC-2020-CRE-0325).

References

1 K. S. Novoselov, A. K. Geim, S. V. Morozov, D.-E. Jiang, Y. Zhang, S. V. Dubonos, I. V. Grigorieva and A. A. Firsov, *Science*, 2004, **306**, 666–669.
2 X. Li, W. Cai, J. An, S. Kim, J. Nah, D. Yang, R. Piner, A. Velamakanni, I. Jung and E. Tutuc, *Science*, 2009, **324**, 1312–1314.
3 K. Watanabe, T. Taniguchi and H. Kanda, *Nat. Mater.*, 2004, **3**, 404–409.
4 A. Zunger, A. Katzir and A. Halperin, *Phys. Rev. B: Solid State*, 1976, **13**, 5560.
5 C. Lee, H. Yan, L. E. Brus, T. F. Heinz, J. Hone and S. Ryu, *ACS Nano*, 2010, **4**, 2695–2700.
6 V. Podzorov, M. Gershenson, C. Kloc, R. Zeis and E. Bucher, *Appl. Phys. Lett.*, 2004, **84**, 3301–3303.
7 Y. Chen, J. Xi, D. O. Dumcenco, Z. Liu, K. Suenaga, D. Wang, Z. Shuai, Y.-S. Huang and L. Xie, *ACS Nano*, 2013, **7**, 4610–4616.
8 G.-H. Lee, Y.-J. Yu, X. Cui, N. Petrone, C.-H. Lee, M. S. Choi, D.-Y. Lee, C. Lee, W. J. Yoo and K. Watanabe, *ACS Nano*, 2013, **7**, 7931–7936.
9 W. Zhao, Z. Ghorannevis, L. Chu, M. Toh, C. Kloc, P.-H. Tan and G. Eda, *ACS Nano*, 2013, **7**, 791–797.
10 J. Qiao, X. Kong, Z.-X. Hu, F. Yang and W. Ji, *Nat. Commun.*, 2014, **5**, 1–7.
11 J.-H. Chen, C. Jang, S. Xiao, M. Ishigami and M. S. Fuhrer, *Nat. Nanotechnol.*, 2008, **3**, 206–209.
12 F. Xia, V. Perebeinos, Y.-M. Lin, Y. Wu and P. Avouris, *Nat. Nanotechnol.*, 2011, **6**, 179–184.
13 A. Allain, J. Kang, K. Banerjee and A. Kis, *Nat. Mater.*, 2015, **14**, 1195–1205.
14 A. K. Geim and I. V. Grigorieva, *Nature*, 2013, **499**, 419–425.
15 K. Novoselov, O. A. Mishchenko, O. A. Carvalho and A. C. Neto, *Science*, 2016, 353.
16 K. Keyshar, Y. Gong, G. Ye, G. Brunetto, W. Zhou, D. P. Cole, K. Hackenberg, Y. He, L. Machado and M. Kabbani, *Adv. Mater.*, 2015, **27**, 4640–4648.
17 C. Ahn, J. Lee, H. U. Kim, H. Bark, M. Jeon, G. H. Ryu, Z. Lee, G. Y. Yeom, K. Kim and J. Jung, *Adv. Mater.*, 2015, **27**, 5223–5229.
18 A. M. Hussain, G. A. T. Sevilla, K. R. Rader and M. M. Hussain, *International Electronics, Communications and Photonics Conference (SIECPC)*, 2013, pp. 1–5.
19 H. Liu, A. T. Neal, Z. Zhu, Z. Luo, X. Xu, D. Tománek and P. D. Ye, *ACS Nano*, 2014, **8**, 4033–4041.
20 J.-S. Kim, Y. Liu, W. Zhu, S. Kim, D. Wu, L. Tao, A. Dodabalapur, K. Lai and D. Akinwande, *Sci. Rep.*, 2015, **5**, 1–7.
21 K. Biswas, L. D. Zhao and M. G. Kanatzidis, *Adv. Energy Mater.*, 2012, **2**, 634–638.
22 N. Dhar, N. Syed, M. Mohiuddin, A. Jannat, A. Zavabeti, B. Y. Zhang, R. S. Datta, P. Atkin, N. Mahmood and D. Esrafilzadeh, *ACS Appl. Mater. Interfaces*, 2018, **10**, 42603–42611.
23 D. J. Riley, J. P. Waggett and K. U. Wijayantha, *J. Mater. Chem.*, 2004, **14**, 704–708.
24 R. Vogel, P. Hoyer and H. Weller, *J. Phys. Chem.*, 2002, **98**, 3183–3188.
25 Z. Zhang, W. Wang, L. Wang and S. Sun, *ACS Appl. Mater. Interfaces*, 2012, **4**, 593–597.
26 B. Chen, C. Uher, L. Iordanidis and M. G. Kanatzidis, *Chem. Mater.*, 1997, **9**, 1655–1658.
27 F. Wald, J. Bullitt and R. Bell, *IEEE Trans. Nucl. Sci.*, 1975, **22**, 246–250.
28 K. Yao, Z. Zhang, X. Liang, Q. Chen, L.-M. Peng and Y. Yu, *J. Phys. Chem. B*, 2006, **110**, 21408–21411.
29 K. A. Messalea, A. Zavabeti, M. Mohiuddin, N. Syed, A. Jannat, P. Atkin, T. Ahmed, S. Walia, C. F. McConville and K. Kalantar-Zadeh, *Adv. Mater. Interfaces*, 2020, **7**, 2001131.
30 M. Xie, J. Zhou, H. Ji, Y. Ye, X. Wang, K. Jiang, L. Shang, Z. Hu and J. Chu, *Appl. Phys. Lett.*, 2019, **115**, 121901.
31 T. Yanase, F. Uehara, I. Naito, T. Nagahama and T. Shimada, *ACS Appl. Nano Mater.*, 2020, **3**, 10462–10469.
32 I. Zumeta-Dube, J.-L. Ortiz-Quiñonez, D. Díaz, C. Trallero-Giner and V.-F. Ruiz-Ruiz, *J. Phys. Chem. C*, 2014, **118**, 30244–30252.
33 J. Grigas, E. Talik and V. Lazauskas, *Phys. Status Solidi B*, 2002, **232**, 220–230.
34 X. Yu, C. Cao and H. Zhu, *Solid State Commun.*, 2005, **134**, 239–243.
35 Y. Zhao, K. T. E. Chua, C. K. Gan, J. Zhang, B. Peng, Z. Peng and Q. Xiong, *Phys. Rev. B: Condens. Matter Mater. Phys.*, 2011, **84**, 205330.
36 Z. Bian, J. Zhu, S. Wang, Y. Cao, X. Qian and H. Li, *J. Phys. Chem. C*, 2008, **112**, 6258–6262.
37 J. Xu, H. Li, S. Fang, K. Jiang, H. Yao, F. Fang, F. Chen, Y. Wang and Y. Shi, *J. Mater. Chem. C*, 2020, **8**, 2102–2108.
38 M. B. Sigman and B. A. Korgel, *Chem. Mater.*, 2005, **17**, 1655–1660.
39 Y. Li, L. Huang, B. Li, X. Wang, Z. Zhou, J. Li and Z. Wei, *ACS Nano*, 2016, **10**, 8938–8946.
40 G. Chen, Y. Yu, K. Zheng, T. Ding, W. Wang, Y. Jiang and Q. Yang, *Small*, 2015, **11**, 2848–2855.
41 A. M. Van Der Zande, P. Y. Huang, D. A. Chenet, T. C. Berkelbach, Y. You, G.-H. Lee, T. F. Heinz, D. R. Reichman, D. A. Muller and J. C. Hone, *Nat. Mater.*, 2013, **12**, 554–561.
42 F. Reale, P. Palczynski, I. Amit, G. F. Jones, J. D. Mehew, A. Bacon, N. Ni, P. C. Sherrell, S. Agnoli and M. F. Craciun, *Sci. Rep.*, 2017, **7**, 1–10.
43 X. He, F. Liu, P. Hu, W. Fu, X. Wang, Q. Zeng, W. Zhao and Z. Liu, *Small*, 2015, **11**, 5423–5429.
44 K. Keyshar, Y. Gong, G. Ye, G. Brunetto, W. Zhou, D. P. Cole, K. Hackenberg, Y. He, L. Machado and M. Kabbani, *Adv. Mater.*, 2015, **27**, 4640–4648.
45 F. Lu, R. Li, Y. Li, N. Huo, J. Yang, Y. Li, B. Li, S. Yang, Z. Wei and J. Li, *ChemPhysChem*, 2015, **16**, 99–103.
46 K. A. Messalea, A. Zavabeti, M. Mohiuddin, N. Syed, A. Jannat, P. Atkin, T. Ahmed, S. Walia, C. F. McConville and K. Kalantar-Zadeh, *Adv. Mater. Interfaces*, 2020, **7**, 2001131.

47 I. Efthimiopoulos, J. Kemichick, X. Zhou, S. V. Khare, D. Ikuta and Y. Wang, *J. Phys. Chem. A*, 2014, **118**, 1713–1720.
48 A. Rawat, N. Jena and A. De Sarkar, *J. Mater. Chem. A*, 2018, **6**, 8693–8704.
49 G. Kresse and J. Furthmüller, *Comput. Mater. Sci.*, 1996, **6**, 15–50.
50 J. P. Perdew, K. Burke and M. Ernzerhof, *Phys. Rev. Lett.*, 1996, **77**, 3865.
51 S. Grimme, J. Antony, S. Ehrlich and H. Krieg, *J. Chem. Phys.*, 2010, **132**, 154104.